remote sensing

MDPI

Article

Measuring Coastal Subsidence after Recent Earthquakes in Chile Central Using SAR Interferometry and GNSS Data

Felipe Orellana [1,*], Joaquín Hormazábal [2], Gonzalo Montalva [3] and Marcos Moreno [4]

[1] Department of Civil, Building and Environmental Engineering, Sapienza University of Rome, 00184 Rome, Italy
[2] Department of Geophysics, FCFM, University of Chile, Santiago 8370449, Chile; joaquin.hormazabal@ug.uchile.cl
[3] Department of Civil Engineering, University of Concepcion, Concepcion 4070409, Chile; gmontalva@udec.cl
[4] Department of Geophysics, University of Concepcion, Concepcion 4091124, Chile; marcosmoreno@udec.cl
* Correspondence: felipe.orellana@uniroma1.it

Abstract: Coastal areas concentrate a large portion of the country's population around urban areas, which in subduction zones commonly are affected by drastic tectonic processes, such as the damage earthquakes have registered in recent decades. The seismic cycle of large earthquakes primarily controls changes in the coastal surface level in these zones. Therefore, quantifying temporal and spatial variations in land level after recent earthquakes is essential to understand shoreline variations better, and to assess their impacts on coastal urban areas. Here, we measure the coastal subsidence in central Chile using a multi-temporal differential interferometric synthetic aperture radar (MT-InSAR). This geographic zone corresponds to the northern limit of the 2010 Maule earthquake (Mw 8.8) rupture, an area affected by an aftershock of magnitude Mw 6.8 in 2019. The study is based on the exploitation of big data from SAR images of Sentinel-1 for comparison with data from continuous GNSS stations. We analyzed a coastline of ~300 km by SAR interferometry that provided high-resolution ground motion rates from between 2018 and 2021. Our results showed a wide range of subsidence rates at different scales, of analyses on a regional scale, and identified the area of subsidence on an urban scale. We identified an anomalous zone of subsidence of ~50 km, with a displacement <−20 mm/year. We discuss these results in the context of the impact of recent earthquakes and analyze the consequences of coastal subsidence. Our results allow us to identify stability in urban areas and quantify the vertical movement of the coast along the entire seismic cycle, in addition to the vertical movement of coast lands. Our results have implications for the planning of coastal infrastructure along subduction coasts in Chile.

Keywords: coastal subsidence; subduction zone; MT-InSAR; GNSS; Sentinel-1

check for updates

Citation: Orellana, F.; Hormazábal, J.; Montalva, G.; Moreno, M. Measuring Coastal Subsidence after Recent Earthquakes in Chile Central Using SAR Interferometry and GNSS Data. *Remote Sens.* **2022**, *14*, 1611. https://doi.org/10.3390/rs14071611

Academic Editors: Guido Ventura and Fabio Matano

Received: 7 February 2022
Accepted: 14 March 2022
Published: 28 March 2022

Publisher's Note: MDPI stays neutral with regard to jurisdictional claims in published maps and institutional affiliations.

Copyright: © 2022 by the authors. Licensee MDPI, Basel, Switzerland. This article is an open access article distributed under the terms and conditions of the Creative Commons Attribution (CC BY) license (https://creativecommons.org/licenses/by/4.0/).

1. Introduction

Chile is one of the most seismic countries in the world [1], where Chile's seismicity and tectonics are characterized by the subduction of the oceanic Nazca Plate below the continental lithosphere of South America (Figure 1) [2]. As a result of the influence of an active subduction margin, Chile has a high and varied level of natural threats resulting from a variety of geomorphological and geological processes. Therefore, the Chilean coast is a geographical area of dynamic terrestrial processes, by definition a highly dynamic area which is constantly in a condition of extreme fragility from high seismic activity. Along the coast of central Chile, the 2010 Maule (Mw 8.8), its aftershocks, and postseismic deformation have dramatically impacted the coastal relief [3–5] over more than 500 km. The relief changes generated by the coseismic coastal uplift, such as the emersion of the marine abrasion platform, widening of beaches, and drying of wetlands, had an important impact on the intertidal biota and anthropic activities [6]. The exposure and risk are

also considerable since many cities, some of them densely populated, are located in high-risk areas [7]. Along with surface level changes, coasts are being affected by climate change, which may increase sea level in the coming decades. Therefore, quantifying with high resolution the impact of recent earthquakes on the coast is of vital importance to understand the processes that control the stability of the coastline. In this context, coastal cities constitute highly vulnerable areas due to the occurrence of threats of marine and continental origin, originating from endogenous and exogenous processes.

The main natural phenomena responsible for the land level changes along coastal areas arise from deeper-lying processes caused by tectonic movements [8,9], such as near-instantaneous coseismic displacements, or slow rates of vertical motions in the interseismic and postseismic periods. These processes produce large-scale deformations involving regional scale effects. Intersismic and postseismic deformations induce low subsidence or uplift rates, thus they do not involve situations of immediate risk, and the effects are observed after several years; however, over a period of several years their effects can change the coastal morphology. On the other hand, subsidence in many cases is caused by the exploitation of groundwater [10–12] and of hydrocarbons [13–15] which imply subsidence at a regional level. Furthermore, much faster anthropogenic causes may be related with urbanization, typically on unconsolidated alluvial deposits, and are usually superficial processes [16,17].

Therefore, the coastal land level is affected by these types of phenomena; that is, land deformation and subsidence or uplift arising from both deep and superficial processes. The quantitative evaluation of subsidence and soil displacement that affects the coast can be carried out based on terrestrial instrumentation and traditional measurement techniques (related to surveying/geodesy), e.g., levelling and GPS, provided that reliable measurements to monitor subsidence are possible in various places [18]; however, these are limited in terms of producing high spatial resolution maps of surface displacement over wide areas. MT-InSAR technology is an alternative solution that can be fully assimilated to terrestrial monitoring [19]. Subsidence monitoring with MT-InSAR takes advantage of the amount of available data that is acquired more frequently and accurately at low cost, and such characteristics make it an attractive source of information [20].

The technology used in this research is based on advanced MT-InSAR approaches [21–24], which consist of exploiting SAR acquisition sequences collected over long periods of time, acquired in the same geometry; we can use these data to provide useful information on spatial and temporal patterns or displacements detected by generating time series with centimeter-to-millimeter precision [25,26]. The MT-InSAR technique is an extension of the traditional InSAR technique involving pairs of images, and allows us to measure subcentimeter ground displacements with millimeter precision, using the phase difference between a series of multiple SAR images that it acquires at different times in the same scene [27]. The MT-InSAR deformation time series have been largely exploited in a wide variety of geophysical contexts, such as seismic, volcanic, and mass movement scenarios, with a dual objective: to map and monitor detected displacements over large areas [28–32]. One of the main attractions of satellite-based MT-InSAR is its ability to cover very large areas remotely at a systematic and continuous rate, making it suitable for regional scale monitoring, as a control tool [33–35], or even as infrastructure networks [19].

In the last decade, many studies around the world have addressed coastal subsidence using differential interferometry to explain and analyze coastal dynamics. Some researchers have integrated MT-InSAR techniques with sea level rise [36–39], mainly addressing environmental processes and climate change. Other studies address subsidence as a result of coastal urbanization, mainly due to the extraction of groundwater [40–42].

In this study, multi-temporal differential interferometry MT-InSAR is used, in addition to the big data of Sentinel-1 in C band coming from the ESA (European Space Agency). We were able to process multiple SAR images using the P-SBAS (Parallel Small BAseline Subset) algorithm [43–46], an evolution of the traditional SBAS (Small BAseline Subset) method [47] developed by the CNR–IREA (Italian Institute of remote sensing for the environment).

The approach used is based on the detection of persistent scatterers (PS) targets that allow the production of projected mean strain rate line-of-sight (LOS) maps and corresponding displacement time series by exploiting interferograms characterized by a small temporal and/or spatial separation (baseline) between the acquisition orbits.

The methodology of this study aims to show the coastal subsidence of central Chile, using the SAR interferometry technique and processing open big data from Sentinel-1, through the iCloud platform (GEP) [48–51]. The method focuses on the presentation of MT-InSAR results, the time series, the comparison with GNSS data, and the geodynamic interpretation of the coastal subsidence phenomenon in Chile. We also compare the MT-InSAR and GNSS-derived displacements of stations mainly from the coast, which is our study area. The displacements along the LOS, in addition to the vertical and EW displacements of the subsidence area, mainly the urban area, were analyzed.

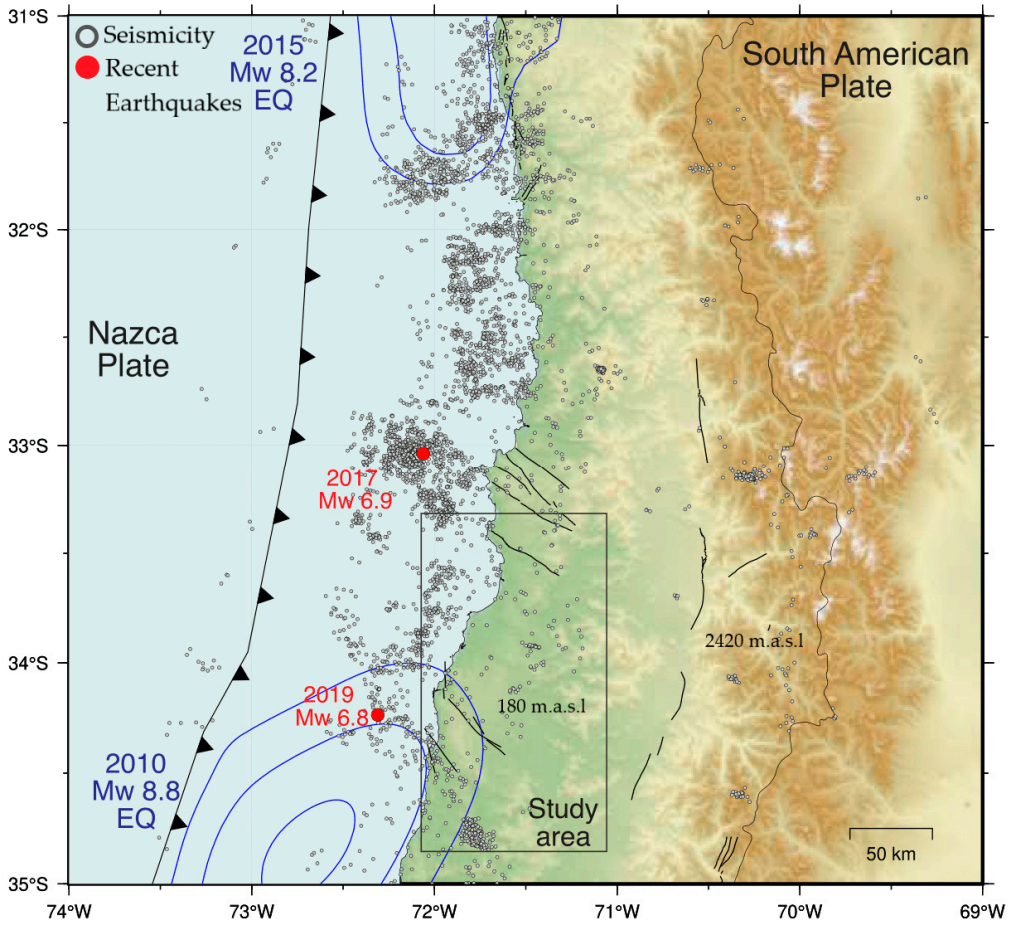

Figure 1. Tectonic setting of the study area. Blue contours indicate the slip of earthquakes that occurred in 2010 (Mw 8.8) and 2015 (Mw 8.2). Gray dots show background seismicity (earthquakes smaller than Mw 6.5) recorded in the study area between 2014 and 2018 [52]. Two earthquakes of magnitudes greater than Mw 6.5 have been recorded in recent years (red dots) [53].

2. Study Area

The study area extending between 33.75° S and 34.75° S is located on the area's northern boundary affected by the 2010 earthquake. This zone is characterized by the existence of active crustal faults (Figure 1). This is demonstrated by the pair of earthquakes (magnitude Mw 6.9 and 7.0) that occurred one week after the 2010 mainshock [54]. During the observation period analyzed in this paper, an earthquake of magnitude Mw 6.8 occurred in August 2019. This event is a reverse earthquake, a typical quake occurring at the interface between tectonic plates (Figure 1).

The study area is along the coast between Valparaiso and Pichilemu. The landscape in this region is defined by the coastal range and the deltas of the rivers that are born in the Andes range. Its main urban center is Pichilemu; other small coastal towns are Navidad, La Estrella, Marchigue, Litueche, and Paredones (Figure 2). As a result of the tectonic configuration of central Chile and the orogenesis of the Andes, the study area presents three well-differentiated morphostructural zones, which from west to east are the Coast Range or Cordillera de la Costa, the Central Depression, and the Main Range or Cordillera de los Andes.

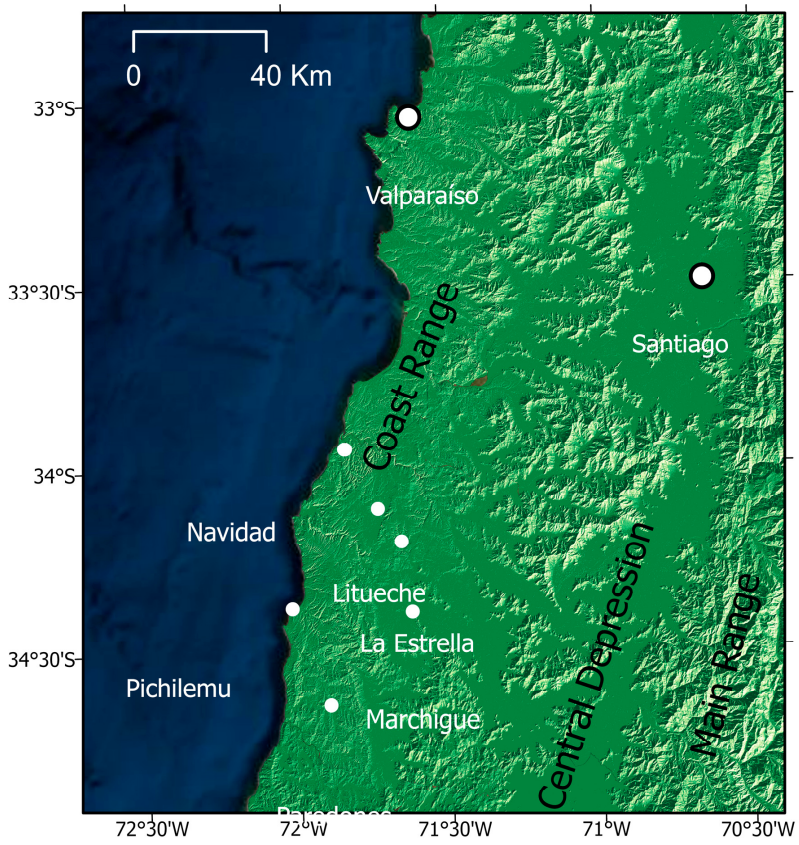

Figure 2. Study area and location of urban areas: Navidad, Litueche, La Estrella, Marchigue, Paredones, and Pichilemu; Coast Range, Central Depression, and Main Range. Background DTM ALOS 30 mts.

Geological Setting

The geology of the study area is characterized by the presence of plutonic bodies associated with the Coastal Batholith; their ages vary from the Upper Paleozoic to the Upper Jurassic. These plutonic bodies are aligned in NW-SE direction stripes. On the other hand, volcanic sequences and to a lesser extent sediment with ages ranging from the Jurassic to the Lower Cretaceous are recognized. In most of the Paleozoic units, foliation has been registered in a NW-SE direction and keeping towards the SW [55]. As for the eastern section of the study area, it is characterized by the presence of a series of stratified sequences of NS orientation and with ages that vary from the Upper Jurassic to the Lower Cretaceous. These units are intruded by Jurassic and Cretaceous granitoids (see Figure 3).

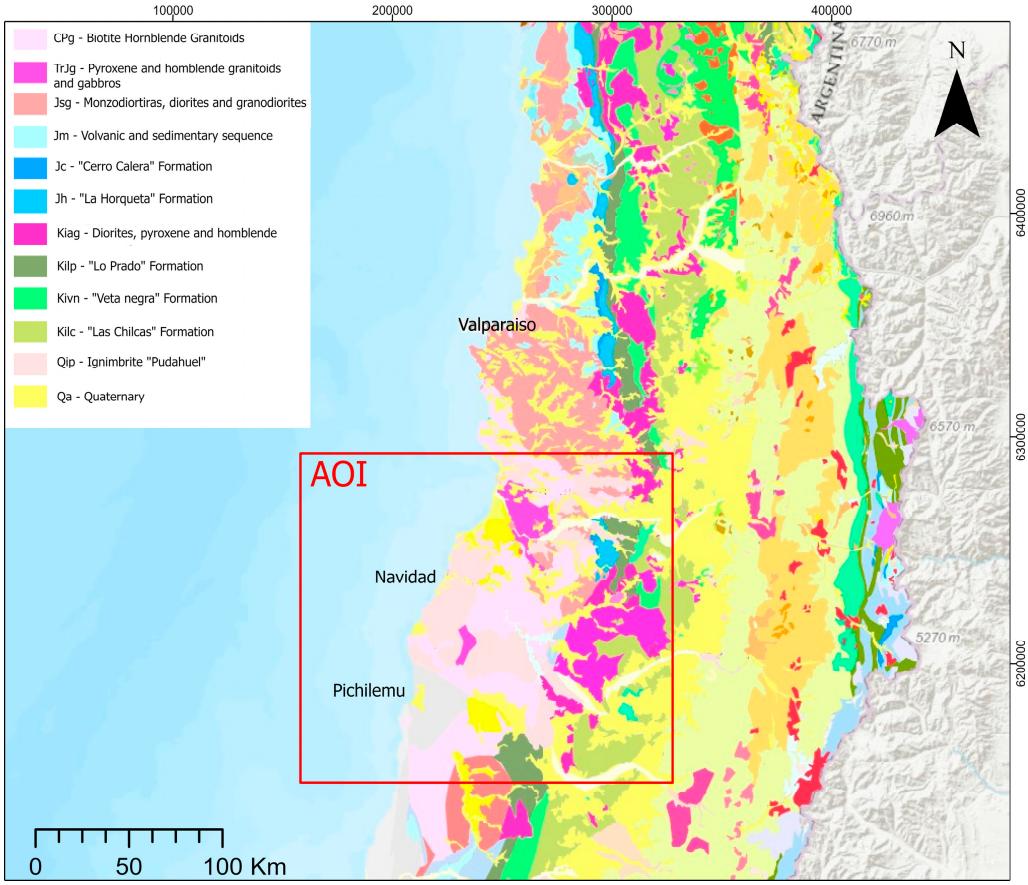

Figure 3. Simplified geological map of Chile central, with main geologic units [56].

The Paleozoic units correspond to large plutonic bodies that are distributed along the western slope of the Cordillera de la Costa. Its lithology consists mainly of tonalites, granodiorites and monzogranites from amphibole and biotite. In addition, metamorphic rocks are found, of plutonic protolith with tectonic foliation [55]. Triassic intrusive rocks occur in the SW zone of the study area. The lithology consists mainly of gneissic diorites, amphibolites, quartz diorites, and partially metamorphosed gabros; they present ductile gneissic foliation, with a NW orientation keeping towards the south. The most voluminous intrusive units correspond to the Jurassic granitoids. The lithology varies between granite, tonalite, granodiorite, and gabros to a lesser extent; towards the westernmost sectors there is a ductile NW-SE foliation; towards this, foliation decreases progressively. Intrusive Cretaceous outcrops are on the eastern slopes of the Cordillera de la Costa. They are plutonic granitoids that intrude both Jurassic intrusives and volcanic and sedimentary rocks of Jurassic and Cretaceous ages [57].

The Cretaceous units correspond to the Lo Prado, Veta Negra, and Las Chilcas formations. The first is arranged in a concordant way on the Horqueta Formation, and consists largely of siliceous volcanic rocks (rhyolites and ignimbrites) [58,59], with volcanic rocks of a maphic character towards the roof of the sequence. The Lo Prado Formation is covered by the Veta Negra Formation, which is made up of a large volume of basaltic to andesitic–basaltic volcanic rocks. The Veta Negra Formation underlies the Las Chilcas Formation in angular unconformity, which corresponds to a volcanic and continental sedimentary sequence, approximately 3000 m thick [60,61]. The Las Chilcas Formation underlies the Lo Valle Formation in unconformity of erosion [57], which corresponds to a pyroclastic sequence of andesitic to rhyolitic composition, with intercalations of lavas and continental sedimentary rocks reaching 1800 m thick [60].

3. Materials and Methods

3.1. Data Set: SAR Imagery

A total of 320 SAR Sentinel-1 images operating in C band were used, covering the period of January 2018–May 2021, using ascending and descending orbits. We limit our analysis to Sentinel-1 data only (12-day repeat cycle) (Table 1), which is considered sufficient given the expected magnitude of ground displacements and the availability of a large file on the study area. The advantages of Sentinel-1 come from its wide range of coverage (250 km swath in wide interferometric mode) and sufficient spatial resolution for large areas (90 m × 90 m range vs. azimuth, for this case). The wide interferometric fringe (IW) acquisition mode is based on the ScanSAR terrain observation mode with progressive scans (TOPS) [62]. The width of the IW 1–3 swath was 250 km, and the angle of incidence of the line of sight (LOS) ranged between 31 and 46 degrees from the near to far range (i.e., ~39 degrees in the center of the scene). Using GEP, SAR images are retrieved, such as Single Look Complex (SLC) data, in addition to SAR images available in the ESA Open Access Hub, ONDA-DIAS, and CREODIAS repositories.

Table 1. Sentinel-1 data set, including the main features of SLC products used.

Orbit	Ascending	Descending
Sensor	1B	1B
N° acquisitions	224	96
Date of measurement start	5 February 2018	10 January 2018
Date of measurement end	26 May 2021	30 May 2021
Relative orbit	18	156
Polarization	VV	VV
Swath	IW 1–3	IW 1–3

3.2. GNSS Data

From this data set we selected the GNSS along the coast of central Chile (Figure 4) from an open access resource using daily solutions processed in the Nevada Geodetic Laboratory (NGL) of the University of Nevada, NV, USA [63], with the time series processed in the IGS14 reference frame [64]. NGL also routinely updates station speeds, the speed, and the path that stations are moving in the global reference frame, which can be used to image displacement rates of the surface deformations.

NGL provides GPS data from more than 17,000 stations around the world and manufactures data products that are multipurpose; for example, the same data can be used to study geodynamics and tectonic deformations. In our case we selected the GNSS stations that are along the coast and we concentrated analysis on the subsidence area using stations RCSD, NAVI, PCMU, and ILOC.

With the continuous improvements of GNSS technology, signals of deformation of the earth's crust, such as deformation of plate boundaries, coseismic static offsets, postseismic deformations lasting for years to decades, and glacial isostatic adjustments have been observed with very accurate results. The description of the temporal evolution of the position of a GNSS station must take into account all these effects, and it has been described using an extended trajectory model (ETM) [65].

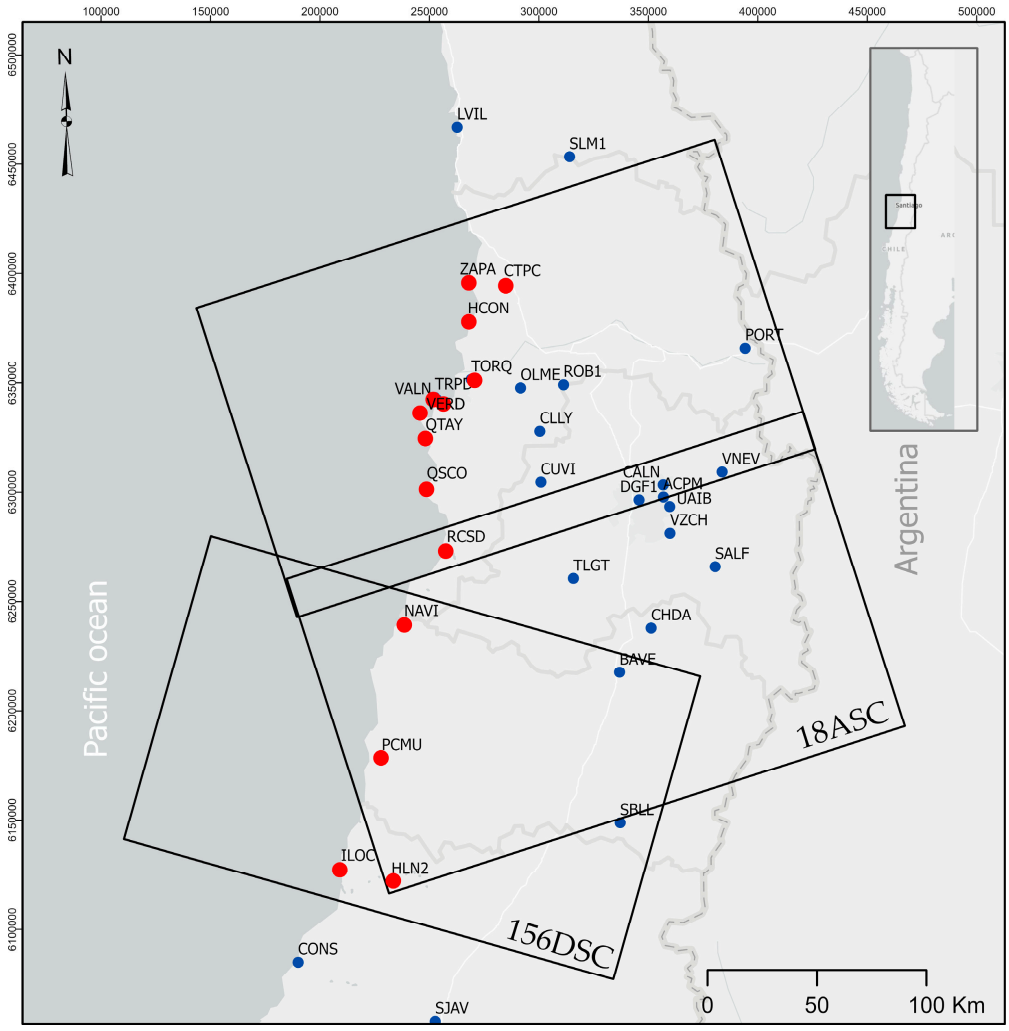

(**a**)

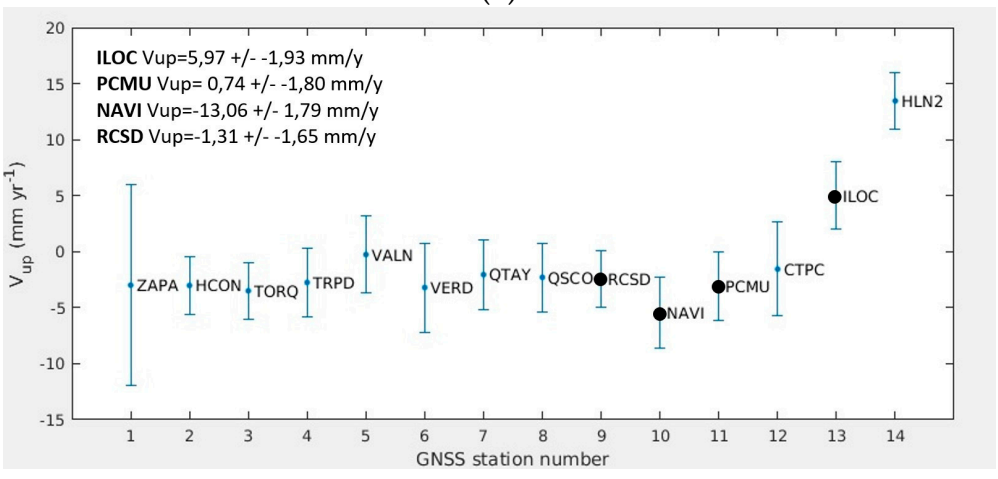

(**b**)

Figure 4. (**a**) Data set used, tracks Sentinel-1 along both relative orbits for ascending (18ASC) and for descending (156DSC), and coastline GPS (red points); (**b**) GPS plot data, with black points representing GPS selected for subsidence areas RCSD, NAVI, PCMU, and ILOC.

3.3. P-SBAS Processing

We adopted the SAR processing that was executed on the ESA iCloud GEP platform, in the service "CNR-IREA P-SBAS Sentinel-1 on-demand processing" v.1.0.0, implemented in

the operating environment based on ESA GRID computing [66]. The processing approach is based on the SBAS technique [47], applied along the ascending and descending orbits of the Sentinel-1 satellites (C-Band SAR sensor wavelength = 5.6 cm); the P-SBAS has been adapted to run efficiently on high-performance distributed computing and configured for Sentinel-1 IW TOPS data processing [45].

The main processing steps of the SBAS approach consist of the generation of differential interferograms from the pairs of SAR images formed with a small orbital separation (spatial baseline) to reduce spatial decorrelation and topographic effects. The Shuttle Radar Topography Mission (SRTM) [67] with NASA's 1 arc-second DEM (~30 m pixel size) and precise orbits from the European Space Agency (ESA) was used for co-registration and for elimination of the topographic phase from the interferometric phase in each of the computational interferograms.

Processing begins with the retrieval of SLC input data from image files, which are primarily based on the ESA Open Access Hub, ONDA DIAS, and CREODIAS repositories. Each stack of SLC data was jointly recorded at the single burst level, ensuring very high joint recording precision (on the order of 1/1000 of the azimuth pixel size), as required for TOPS data due to the large Doppler centroid along the path variations [68]. The next step is the calculation of temporal coherence and the threshold of the minimum temporal coherence, allowed to select coherent targets set at 0.85. Atmospheric phase components were identified and removed. The output data sets that include geolocation (i.e., latitude and longitude in the WGS84 system, and elevation above the reference ellipsoid), annual LOS velocity, and date-by-date offset histories (time series) for each coherent objective values were exported, separated by commas in (.csv) ASCII format, in accordance with the specifications of the European Plate Observing System—Implementation Phase (EPOS—IP) project, where the metadata is standardized to that which corresponds to a set of output data, LOS speed in raster (.png), and Google Earth (.kmz).

The control point for the processing of P-SBAS was established in the same location in the city of Santiago −70,654, −33,443, and in the City of Rancagua −71,648, −33,023, where the annual LOS speed values and the time series were referenced accordingly. The use of a common reference point allowed internal calibration of the two output data sets.

3.4. Post-Processing

Vertical and East-West Deformation Component Estimation

The ascending and descending data sets were combined to obtain the vertical displacement V_u and the V_E east-west velocity field. A 90-meter square element network was used to resample the point data sets in a regular grid and to link the output data sets into a single layer. Both P-SBAS outputs (ascending and descending) were available at the same location i. The combination was achieved under the assumption of negligible north-south velocity, $V_N = 0$. This assumption is typically used in MT-InSAR studies to take into account the relatively poor visibility of north-south horizontal movements that the LOS sensor is limited to [69].

Given the known values of the deformation velocity LOS in the ascending (V_{asc}), descending (V_{dsc}), and the unit vectors (E_{Di} , U_{Di}) modes at each location i, the V_U and V_E were estimated as follows:

$$V_{ui} = \frac{E_{Di} * V_{Ai} - E_{Ai} * V_{Di}}{E_{Di} * U_{Ai} - E_{Ai} * U_{Di}} \quad (1)$$

$$V_{Ei} = \frac{U_{Di} * V_{Di} - U_{Di} * V_{Ai}}{E_{Di} * U_{Ai} - E_{Ai} * U_{Di}} \quad (2)$$

4. Results and Discussion

The results were analyzed using GIS-based cartography (WGS84—UTM zone 19S), with MAXAR images from ESRI source for the background maps. In the first instance we obtained an overview of surface deformation velocity (mm/year); later, we concentrated our analysis on showing the subsidence area, and on analyzing urban centers located along the coast using spatial interpolation techniques and cumulative displacements of MT-InSAR.

Our results show a high agreement between the estimates obtained from InSAR and GNSS. In the observed period, the coast subsided at peak ratios of ~25.00 mm/year. This maximum coincides with the area affected by the aftershock of 1 August 2019 (Mw 6.9). This earthquake demonstrates that a local effect (~20 km area) can produce moderate magnitude earthquakes.

The field of vertical and horizontal displacement of the subsidence area between February 2018 and May 2021 unequivocally highlights that the promontory is affected by land subsidence. The vertical velocity increases from the agricultural zone towards the coast. Despite the lower density of coherent targets throughout the rural landscape, the east-west horizontal field makes it clear that the movements of the earth's crust converged towards the coastal zone; this is the place around which the subsidence seemed to center. Our SAR processing results are available as Supplementary Materials, in .kmz format, they indicate the target-PSI of each frame used.

4.1. Regional Displacement Overview

In this section, we show the regional deformation phenomenon detected by the MT-InSAR analysis in the coast of central Chile, with a length of 300 km effectively covered by SAR data. In order to represent a regional displacement overview, we use big data based on PSI (Persistent Scatterers Interferometry), obtained from interferograms, using total coverage of the Sentinel-1 images, which is 250 km in S-1 IW mode. This allowed us to cover very large areas over the central region of Chile.

The regional displacement is presented in Figure 5. The large data used for the construction of these maps are all from PSI with a coherence >0.85. We obtained maps of more than 5 mls of points for the ascending orbit and 2 mls of points for the descending orbit. It should be noted that to generate this amount of points (PSI), at least 48 h of processing were necessary for each frame. For the classification of the PSI displacement speed we used a range of −20 to 20 (mm/year), for which we detected the area of subsidence in the SW of the analyzed region, indicated in red.

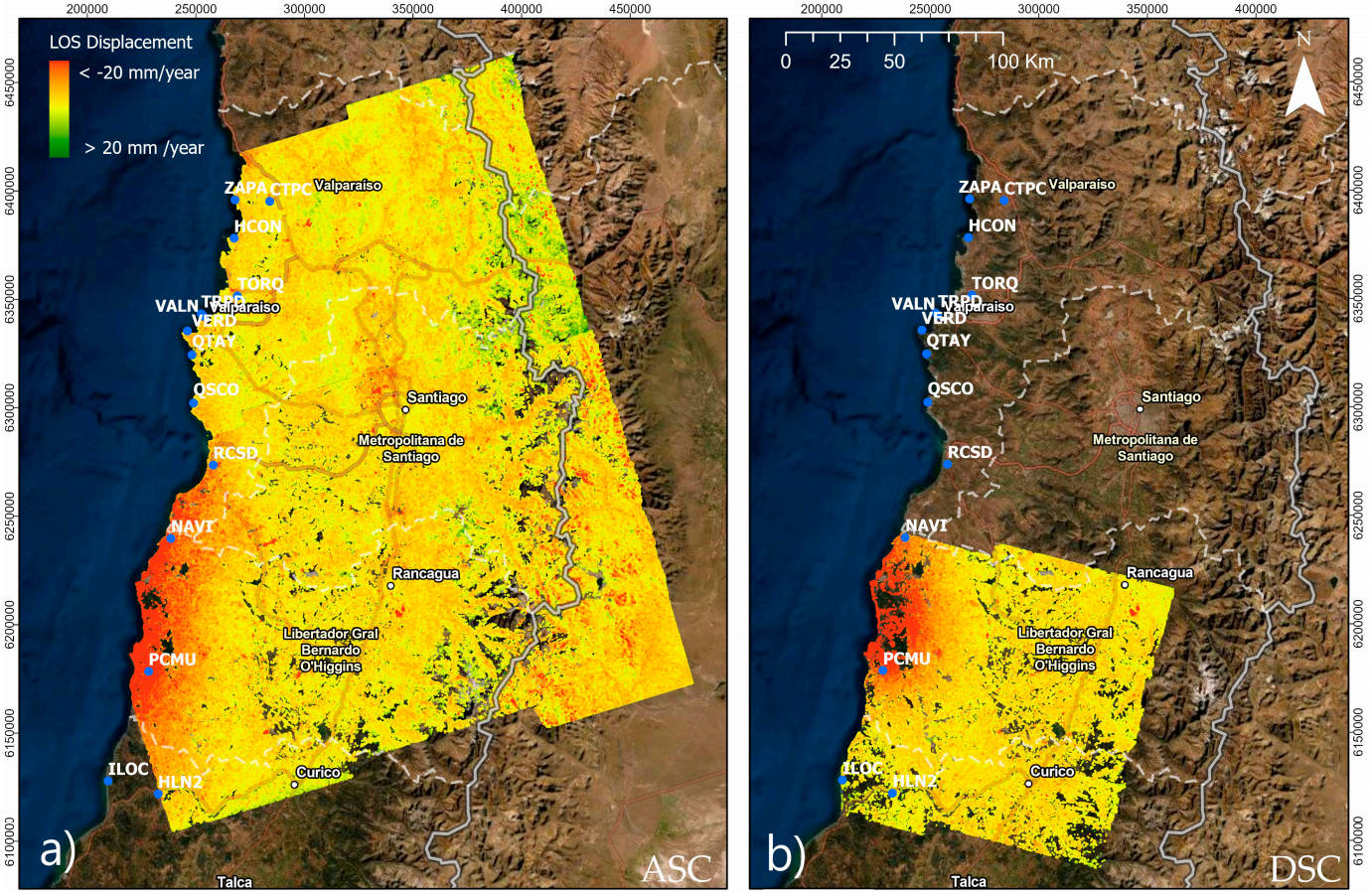

Figure 5. Regional displacement overview maps (mm/year), with (**a**) representing ascending orbit 18ASC and (**b**) descending orbit 156DSC, for the MT-InSAR observation period 2018–2021. The subsidence detected is red for the SW area.

4.2. Subsidence Area

The coastal subsidence area covers ~2000 km^2. The area includes urban districts, such as Pichilemu, and small rural towns such as Navidad, Litueche, La Estrella, Marchigue, and Paredones. The coastline represents a length of 50 km. It is affected mainly by the effects of tectonic subsidence.

To show the subsidence we used both ascending and descending orbits, where a similar spatial density of ~100 PSI/km^2 was detected; however, it can be noted that there is a foreshortening effect, since the descending orbit is less than the slope of the angle out of nadir and tends to be perpendicular to the line of sight (LOS).

The velocities of LOS during January 2018–May 2021 ranged between −57 and +26 mm/year for the upstream data set, and between −40 and +23 mm/year for the downstream data set. Negative velocity values indicate movement away from the satellite sensor (dark red dots), while positive values indicate movement toward the sensor (yellow dots). Figure 6 shows the sink area detected by the ascending and descending orbits.

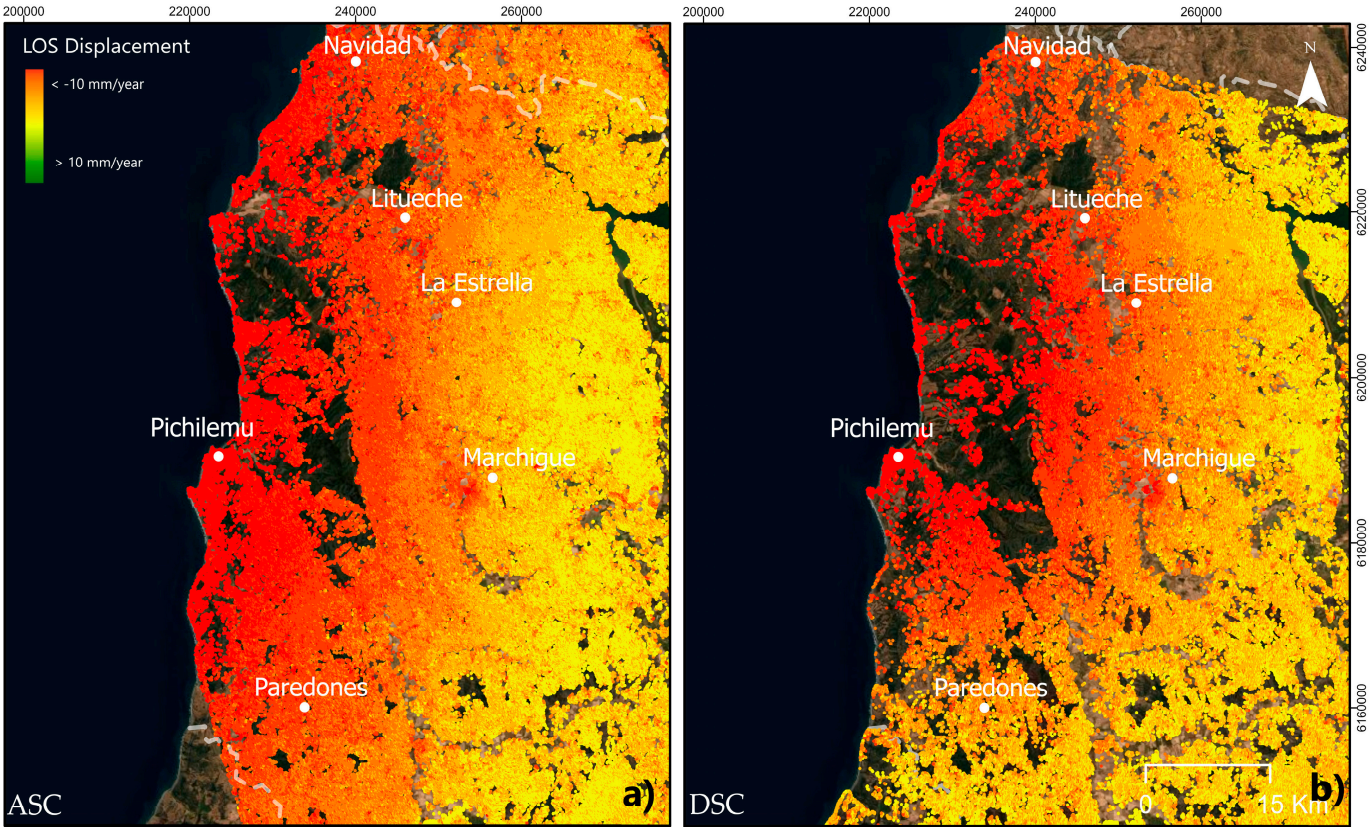

Figure 6. Land displacement maps in subsidence area (mm/year) for (**a**) ascending orbit 18ASC and (**b**) descending orbit 156DSC. Small towns are evidenced by white points.

4.2.1. Time Series Verification

The deformation time series represent the most advanced MT-InSAR product. They provide the history of deformations during the observed period, which is fundamental for many applications to study the kinematics of a given phenomenon (failures, activation, acceleration, etc.) and its correlation with inducing factors. In order to properly use, interpret, and exploit the deformation time series, it is important to consider that they are a zero product redundancy. In fact, they contain an estimate of deformation for each SAR acquisition, that is, for each observation. For this reason, they are particularly sensitive to phase noise [70].

The time series of the P-SBAS algorithm have been successfully compared and validated in previous works [45]. For our case and following the results in the subsidence area, we focused on an extended quantitative analysis that assessed the quality of the P-SBAS and GNSS measurements. We present graphs in Figure 7 that show the comparisons and validation between the displacement time series recovered from Sentinel-1 interferometric data developed by the P-SBAS processing chain (red dots), and the corresponding GNSS projected by LOS (black lines) for stations labeled RSCD, NAVI, PCMU, and ILOC. Consistent with the above results, there is very good agreement between the P-SBAS and GNSS measurements projected by LOS.

There are certain types of surface deformation phenomena that InSAR processing chains could not detect as a result of atmospheric noise factors. However, the results obtained by both signals in the LOS show similar displacement trends; for example, for the R^2 of P-SBAS and GPS, NAVI, are 0.75 and 0.73, respectively, also in the PCMU DSC time series. A very similar lag has been detected for both signals, which can be associated with the tectonic process. The closest GNSS station (PCMU) to the earthquake indicated a subsidence of ~30 mm (Figure 7). InSAR spatially complements the surface level change

record, providing a record similar to GNSS but precisely determining the area that subsides by this earthquake.

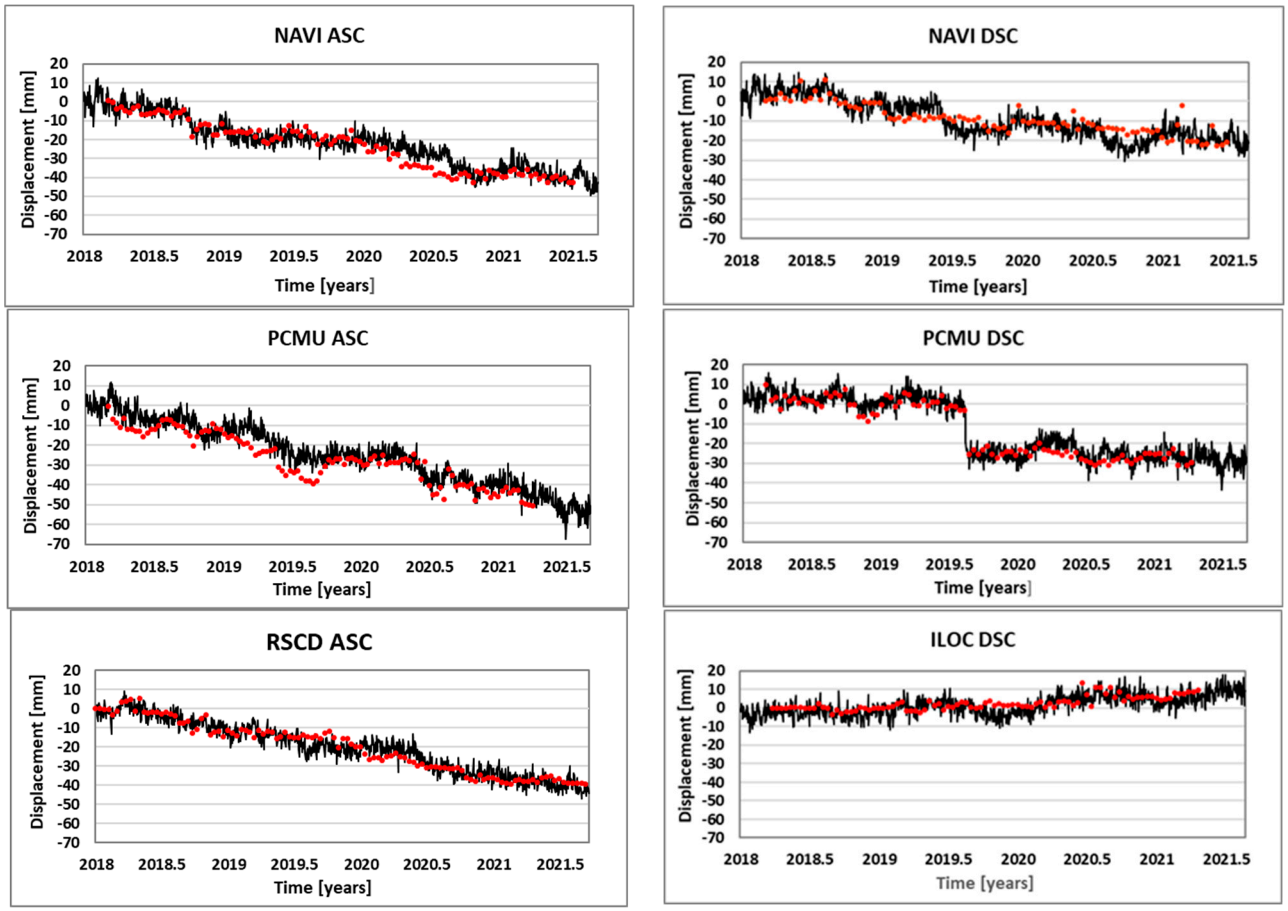

Figure 7. Comparison between the P-SBAS surface deformation time series (red points) and the projected GNSS LOS (black lines) relevant to the stations identified in the subsidence areas NAVI, PCMU, RSCD and ILOC.

4.2.2. Vertical Displacement Estimation

The vertical velocity components (Vup) were calculated after combining the two upstream and downstream data sets, where a 90-square-meter network was used to resample the point data sets on a regular grid and link the output data sets into a single digital layer in SHP format.

The coastal subsidence shows a generalized presence of negative velocities that indicate subsidence, with observed rates of up to −25.00 mm/year (Figure 8). Along the oceanic coast, a subsidence pattern that increases from north to south can be recognized, involving towns such as Navidad and Pichilemu; in addition, the subsidence pattern that increases from east to west can be recognized (Figure 9), which is due to the occurrence of the subduction phenomenon of the Chilean coast. The area of greatest coastal subsidence is between the districts of Navidad and Pichilemu, where the rates reached −25.00 mm/year.

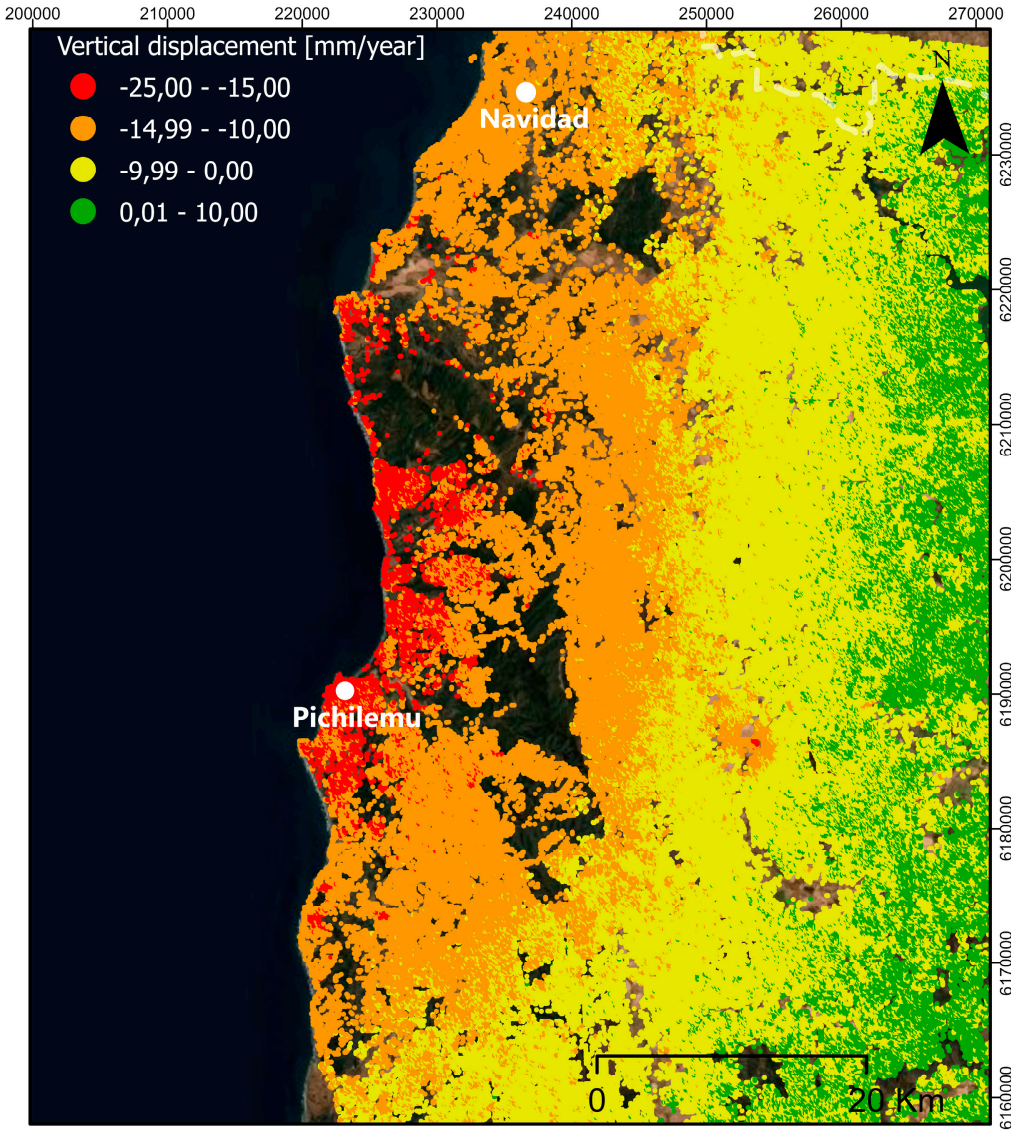

Figure 8. Vertical displacement component estimation map (mm/year) for subsidence area.

4.2.3. E-W Displacement Estimation

The horizontal component EW allowed us to identify common patterns of east-west displacement. The effect of the displacement of the earth's crust towards the west is evidenced mainly in the area of subsidence, with a displacement rate of up to −10.00 mm/year (dark green); in contrast (Figure 9), the eastward shift increases as you move away from the subsistence zone, with shift rates of up to 5.00 mm/year (light color). This relationship of subsidence and velocities to the west can be associated with a postseismic period of the seismic cycle, where there is still a relaxation of stresses after an earthquake. Particularly in this zone a postseismic influence can be appreciated as a result of the Maule 2010 earthquake and possibly as a result of the Pichilemu 2019 earthquake. Even so, it should be noted that the horizontal displacements show that between Navidad and Pichilemu there is a greater postseismic influence, since in this zone the velocities are oriented towards the trench, while the vertical velocities show that the zone is a little wider, which may be related to existing rheological properties in the area.

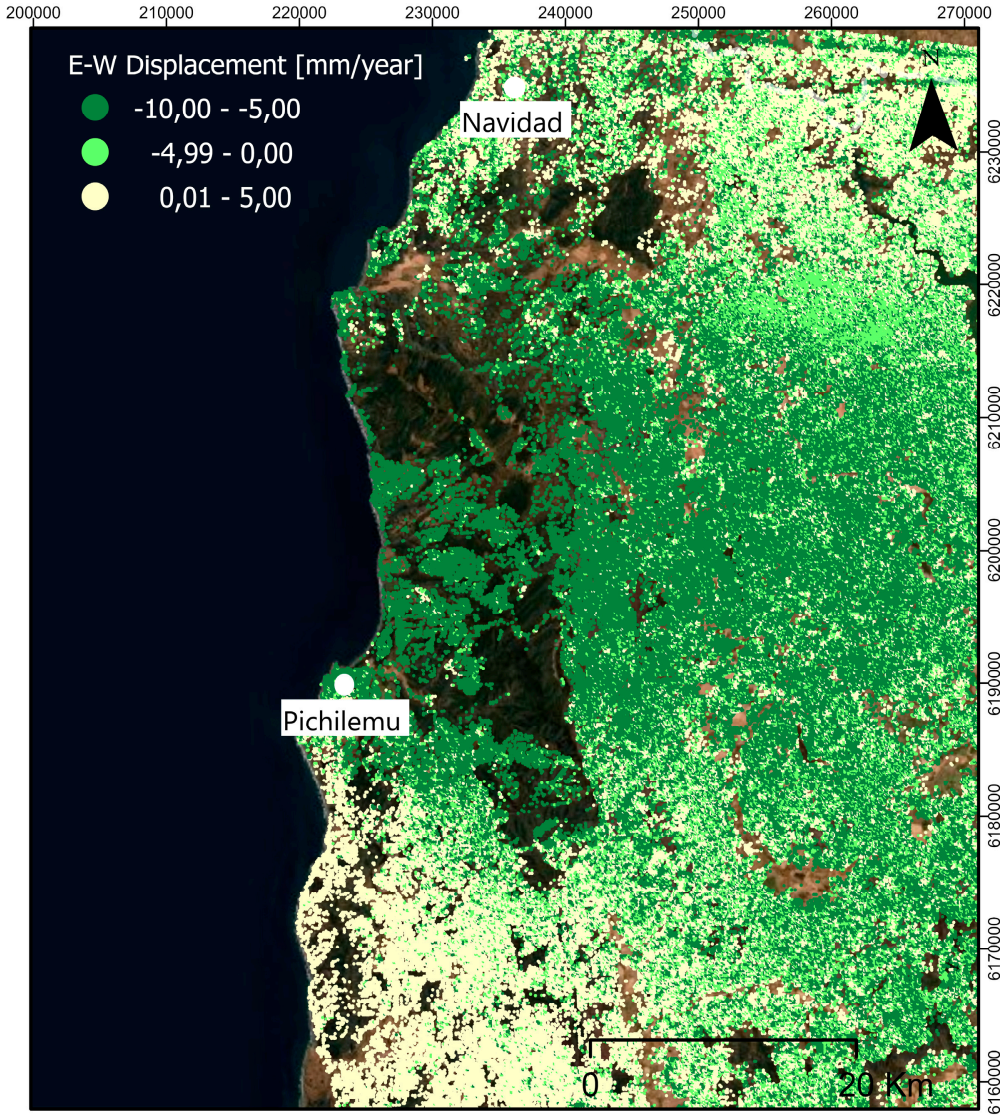

Figure 9. E-W displacement component estimation map (mm/year) for the subsidence area.

4.3. Urban Areas

The area of subsidence includes different municipalities located along the coast. These urban districts are mainly the following: Pichilemu, which is the most important urban center; Paredones, La Estrella, Mirchigue, Litueche, and Navidad. The urban areas were affected by two large earthquakes and their coseismic effects 6.9 (Mw), some of which caused significant changes in the seafloor that could partially explain the changes in the coastline and its dynamics. These changes, coseismic uplift/subsidence obtained from post-tsunami studies, and source inversions, are detailed for these earthquakes and their effects on the coastal areas of Navidad and Pichilemu [71–74], where coseismic changes can be highly variable in space and determined by changes in the coastline. In addition, coseismic subsidence in combination with sea level rise enhances beach erosion, and coastal subsidence can induce accretion [75].

In order to show subsidence areas at urban scales, we use the IDW (Inverse Distance Weighting) interpolation method. The values assigned to the unknown points are calculated with a weighting of the average PSI values available at the known points. In this case we use the input of the vertical displacement value (Vup).

In Figure 10 we classify each of the maps according to the vertical displacement, with a value of up to −25.00 mm/year, where the greatest subsidence occurs on the coast (red

color). Tectonic subsidence is identified within the current urban limits for each of the municipalities and is described in Table 2. The urban infrastructure network, road network, buildings, and primary infrastructure are all exposed to the phenomenon of subsidence.

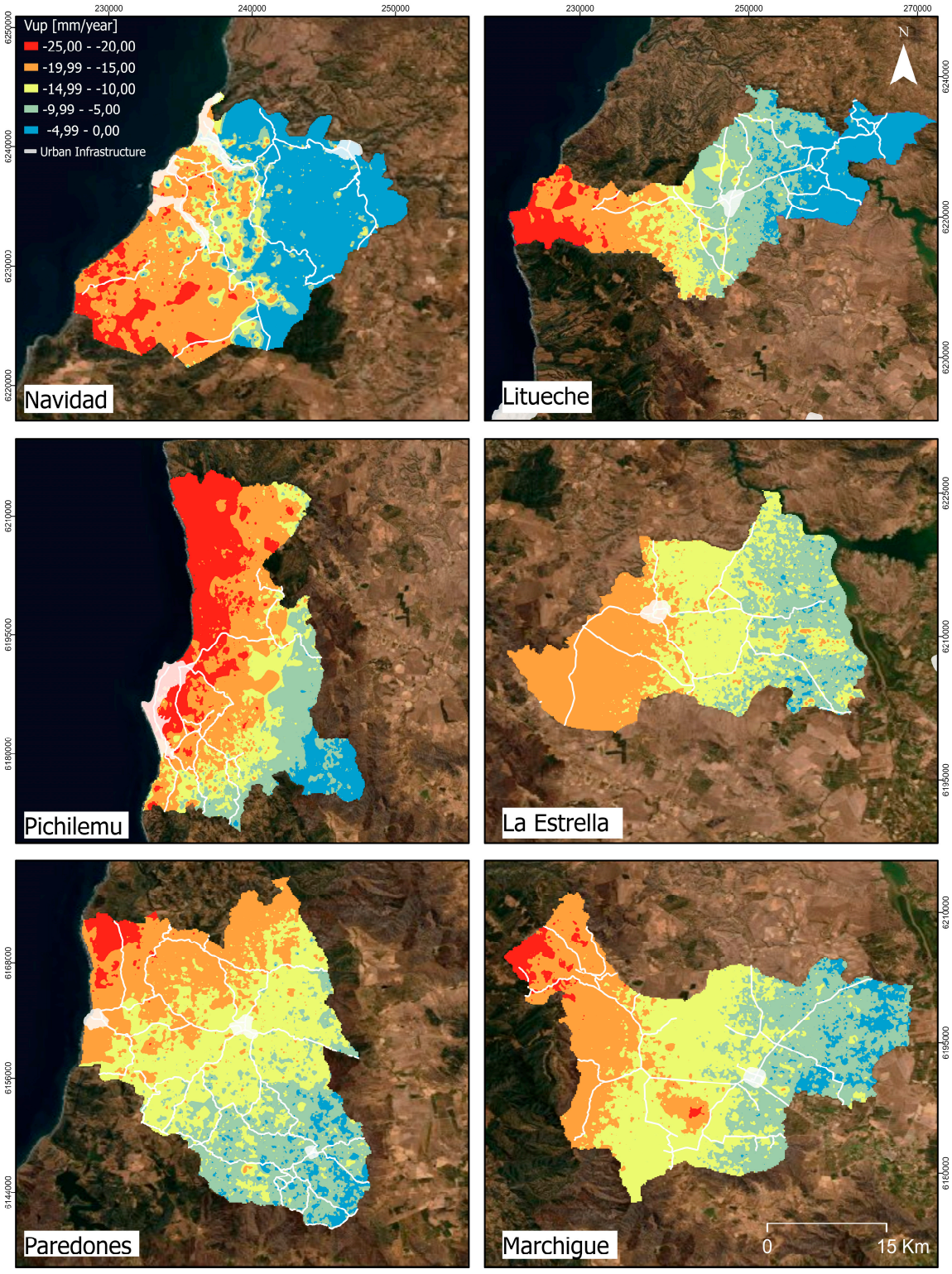

Figure 10. Vertical displacement, Vup maps (mm/year), for each of the municipalities in the subsidence area (Navidad, Pichilemu, Paredones, Litueche, La Estrella, and Marchigue).

Table 2. Basic statistics of PSI MT-InSAR for municipalities.

Municipalities	Count PSI	Min	Max	Mean	Standard Deviation	Subsidence Area km^2	R^2
Navidad	52,659	−2.70	0.68	−0.65	0.62	44.13	0.89
Litueche	60,676	−3.42	0.58	−1.09	0.72	58.35	0.85
Pichilemu	50,250	−3.28	−0.23	−2.00	0.50	231.07	0.77
La Estrella	45,827	−1.92	0.56	−0.33	0.39	0.00	0.00
Paredones	48,077	−2.84	0.18	−0.83	0.42	17.04	0.95
Marchigue	58,816	−2.70	−0.24	−1.43	0.37	16.93	0.90

The morphodynamic effects of the 2010 Mw 8.8 seismic event on the Pichilemu coastline were the extreme erosion of beaches and dunes, leaving as main geomorphological characteristics monosequential erosive beach profiles, with cliffs in previous dune cords on the order of meters high [76]. The coseismic deformation induced by the 2010 earthquake caused a general retreat and subsidence of the coast [3]. Currently the urban center of Pichilemu is the most exposed to the subsidence zone. This area comprises 158.75 km^2 located along the coast; however, to confirm the level of risk to urban infrastructures, it is necessary to rectify with data and in situ surveys carried out at a local level. The resolution and extent of these maps allow detailed planning for a number of hazards.

For urban areas, the PSI-targets were sufficient to characterize the phenomenon of subsidence. We identified Pichilemu, Litueche, and Navidad as the areas most exposed to coastal subsidence, and observed large rates of vertical displacement (PSI < −20,00). In Table 2 we show the count of PSI-targets for each municipality from the study area, evidencing the negative values of the mean, in addition to a common trend of displacement R^2 for the subsistence areas (km^2).

Navidad and Pichilemu

To interpret the coastal subsidence caused by recent seismic events, we focus on the Navidad and Pichilemu areas, where the subsidence of the area shows settlement of the urban infrastructure interspersed with some larger-scale seismic movement patterns. The geological faults located in the Navidad and Pichilemu areas are part of an intraplate seismic sequence after Maule 2010 (8.8 Mw) [54,72,76], producing a morphological lineament oriented mainly to the NW where a parallel drainage network is clearly inverted to the SW of the surface seismicity projection [77]. According to the CHAF (Chilean Active Fault) database [53], the urban areas of Navidad and Pichilemu are crossed by potentially active faults 1, 2, and 3 (Figure 11).

It is important to point out that the subsidence in this area is not only a result of the coseismic effect of the Mw 6.9 earthquake; in previous years, this area already presented a subsidence of ~5 mm/year as a consequence of postseismic effects of the 2010 event. Furthermore, even after this seismic event this area continues subsidence at a rate of ~10 mm/year. This important observation demonstrates that there was possibly movement on the fault before the earthquake and associated postseismic deformation in subsequent months. In the Navidad and Pichilemu zones, the faults caused by tectonic stresses in the study area have accumulated a potential slip between the crustal blocks separated by the fault in the urban zone. In Figure 12, we can observe part of the coastal surface deformation cycle, where potentially active faults have generated accumulated energy and therefore pose more risk for urban areas.

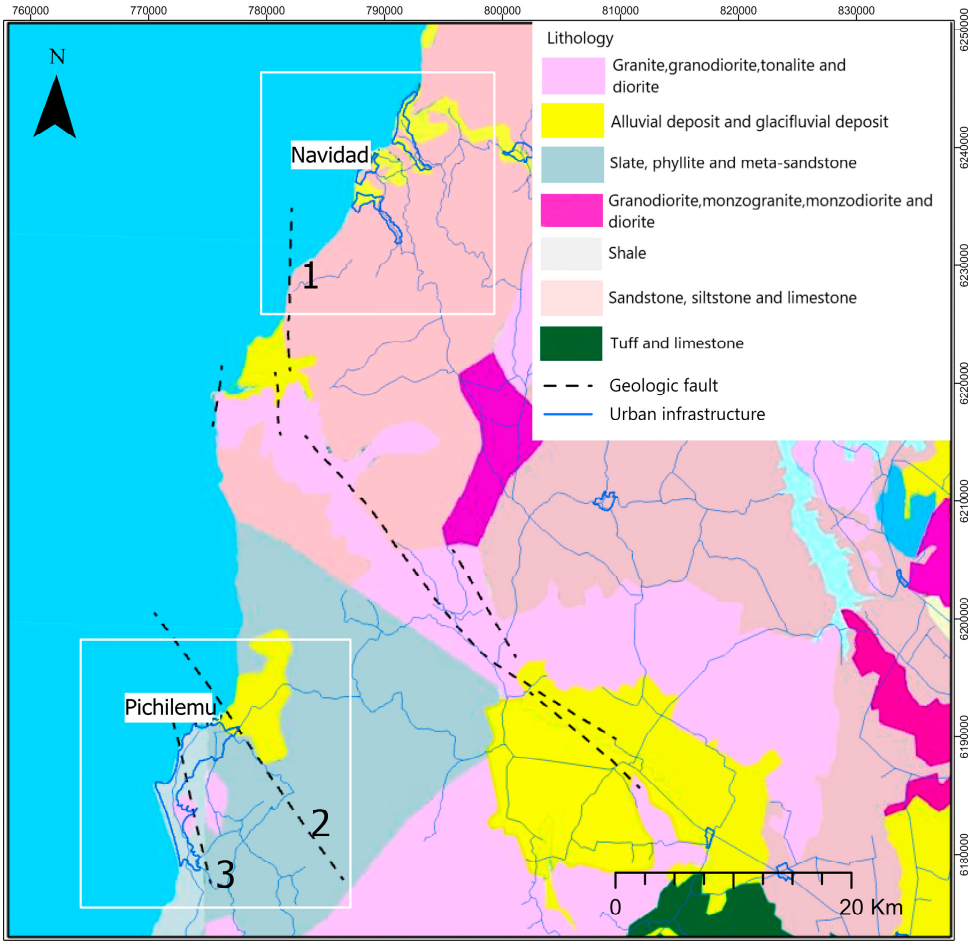

Figure 11. Geological map of the study area for Navidad and Pichilemu, with main lithology [56], black segmented lines for geological faults [53] denominated 1,2, and 3 for the areas of Navidad and Pichilemu, and blue lines denoting urban infrastructure for the study area.

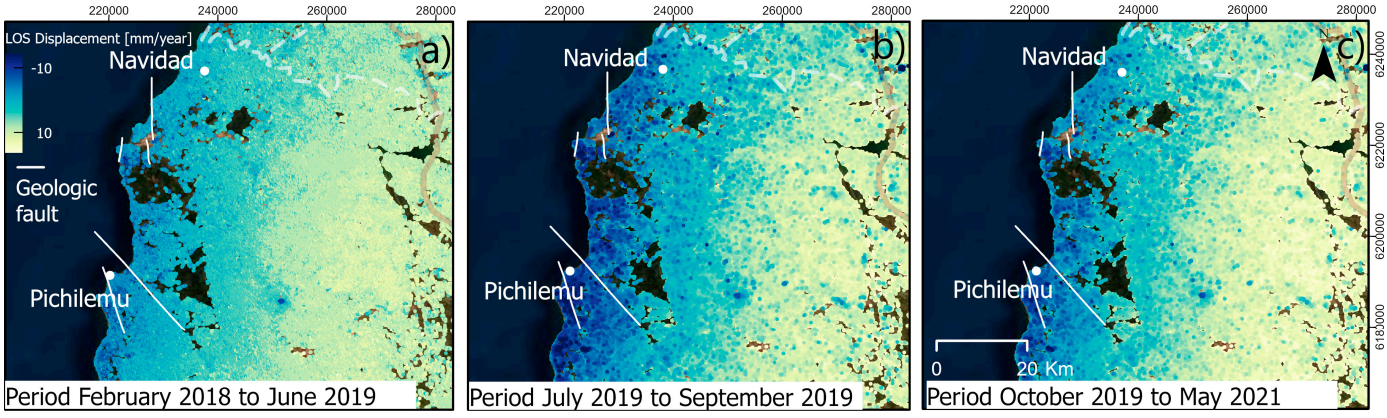

Figure 12. Comparison LOS displacement for Navidad and Pichilemu areas (**a**) pre-earthquake: February 2018–June 2019, (**b**) earthquake: July 2019–September 2019, and (**c**) post-earthquake October 2019–May 2021.

It is essential to show the effect of the faults and the type of soil that predominates urban areas to achieve a correct interpretation of coastal subsidence. The geology of the Navidad and Pichilemu areas features alluvial deposits, sands, and sandstones (Figure 11), mainly on the coast. Although during the observation period we recorded a low intensity earthquake on 1 August 2019 (Mw 6.9), the speeds of the seismic waves can be affected by

the properties of the medium through which they pass, be it the lithology, the presence of fractures, pressure, temperature, and the presence of fluids.

In the case of Navidad we can observe a cumulative displacement from 3 years of observation of values up to −59.99 [mm], oriented towards Fault 1 (Figure 13); in Pichilemu, we can observe accumulated displacement values up to −75.00 [mm] between Faults 2 and 3.

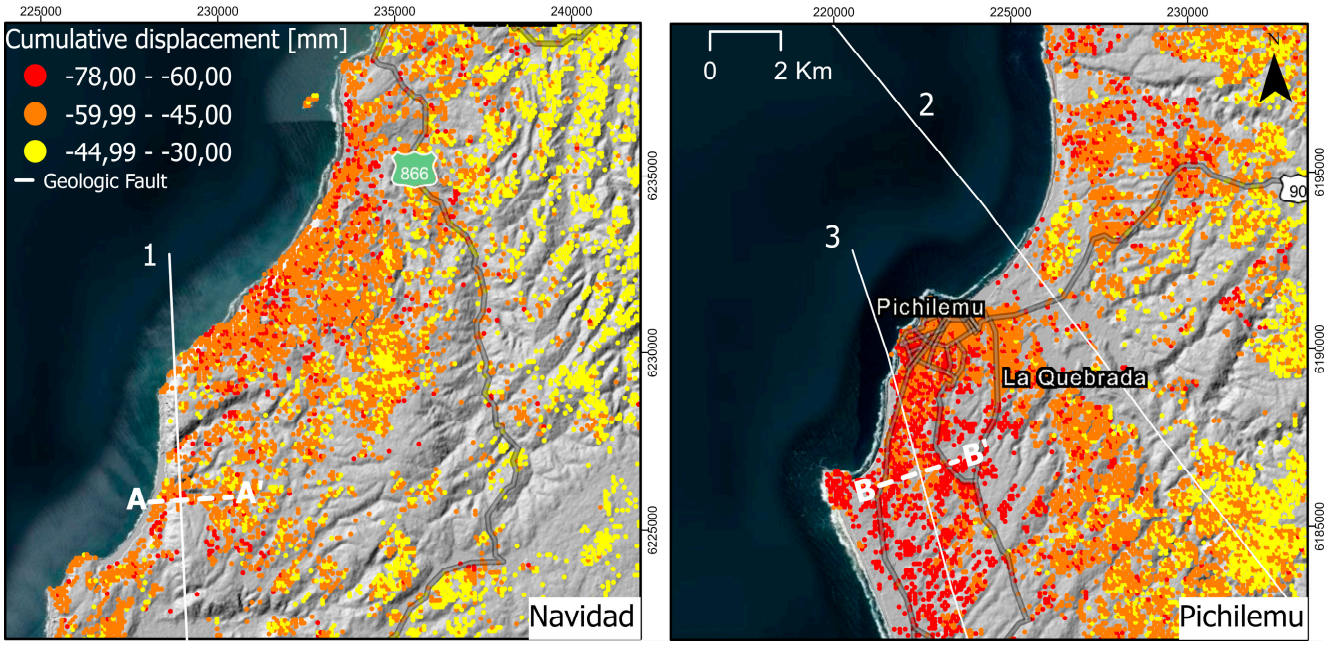

Figure 13. Cumulative displacement maps [mm] for Navidad and Pichilemu; white lines represent geologic faults crossing coastal zone of Navidad and urban area of Pichilemu; background DEM ALOS PalSAR 12.5 mts.

The deformation of the Navidad and Pichilemu areas is strongly controlled by its structural heritage and by its geological characteristics. This is of particular importance for the potential reactivation of crustal structures during and after the occurrence of large subduction earthquakes, and is therefore also critical for seismic hazard assessment [78]. The evolution of the coastline is also strongly associated with erosion caused by large earthquakes and tsunamis; however, it was quickly rebuilt as a result of favorable sedimentary input [75]. This positive evolution has not been observed in the Pichilemu area, although it could be comparable to Navidad since both sectors are very close and have cove morphology; the differences can be understood more by coseismic subsidence, and less by sedimentary contribution.

To evidence the coastal subsidence and the correlations of its faults, we drew a terrain profile (AA′ and B-B′) in Fault 1 and Fault 3, respectively, and compared it with the profiles estimated by MT-InSAR (Figure 14). For this study we noticed that the subsidence areas of the ground are not controlled by faults, but rather by large-scale tectonic subduction; however, the results presented in Figure 14 show us a possible activation of Fault 3 caused by recent earthquake activity.

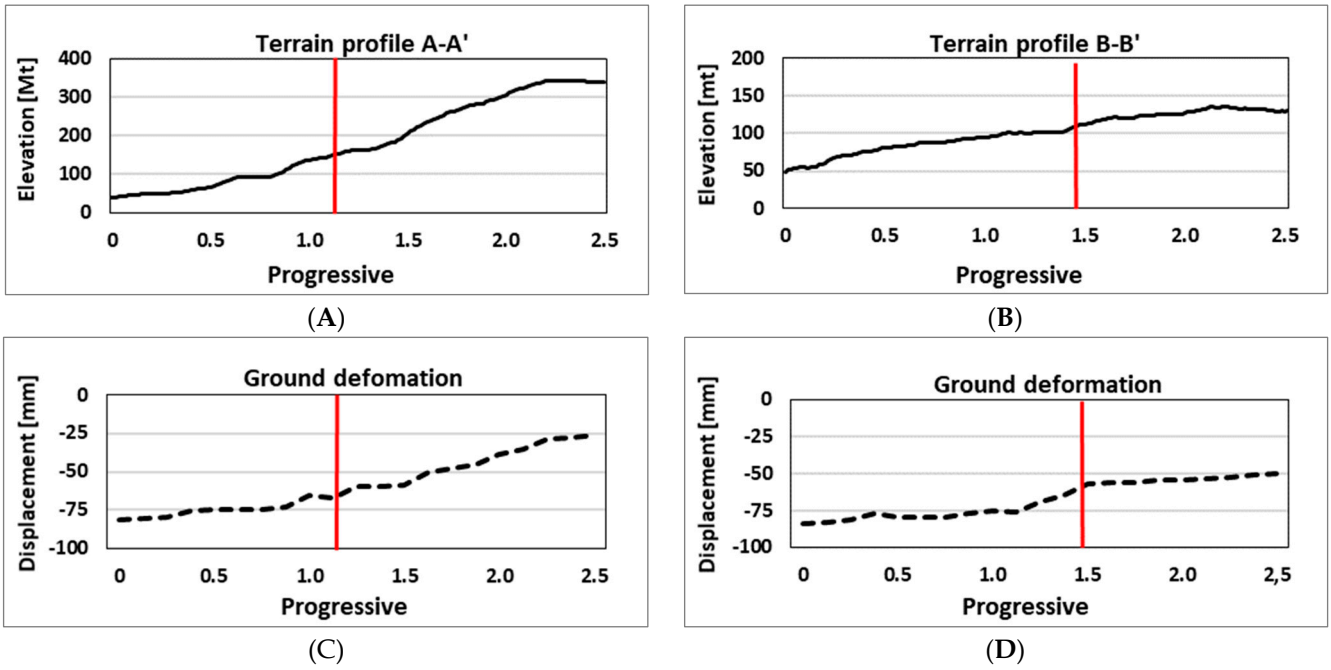

Figure 14. Profile lines are perpendicular to Fault 1 and Fault 3. Figures (**A**) and (**B**) show the terrain profile (A-A', B-B'), and (**C**) and (**D**) show the estimated ground deformation obtained with MT-InSAR.

5. Conclusions

MT-InSAR satellite interferometry techniques have proven to be useful for observing displacements on different spatial scales. The large amount of data available from Sentinel-1 with high frequency has allowed us to create robust interferometric data stacks that cover very wide regions, obtaining very reliable multi-temporal results. It has also allowed us to investigate the large-scale evolution of a coastline; it has also allowed us to investigate displacement at urban scales, and create useful maps for spatial planning.

The results of both orbits of the satellite sensor were shown in a similar way from the point of view of spatial density; however, there is a foreshortening effect for some areas that can be improved by complementing the orbits. The available GNSS data have shown correlations with SAR data, considering that both complementary technologies are reliable, low-cost resources.

We have shown that the deformation of the coastal surface is imposed by the seismic activity of the subduction area on a large scale, and that there are different factors that can enhance the subsidence of urban areas, such as geological faults and soil typology. From the analysis of the data and the cartography, it is concluded that there are tectonic conditions that configure current scenarios and potential threats inherent to a tectonically active seismic coastal zone. We also conclude that in the medium term there may be an increase in risk resulting from greater exposure generated by the protrusion of the urban fabric on dune fields near the coast, susceptible to tsunami flooding or increases in sea level.

To verify the risks associated with the effects of earthquakes and coastal tectonic subsidence in urban centers, it is necessary to complement our information with that obtained from local surveys; however, the results obtained allow us to understand the phenomenon of tectonic subsidence of the Chilean coast in urban areas, detect potentially hazardous areas, and contribute to correct spatial planning.

Supplementary Materials: The following supporting information can be downloaded at: https://www.mdpi.com/article/10.3390/rs14071611/s1. PSI data. kmz for ascending and descending frames + .png image output data.

Author Contributions: Conceptualization, F.O., M.M. and G.M.; methodology, F.O. and M.M.; software, F.O. and J.H.; validation F.O. and J.H.; writing F.O.; supervision, M.M. and G.M. All authors have read and agreed to the published version of the manuscript.

Funding: We acknowledge financial support from the Millennium Nucleus CYCLO (The Seismic Cycle Along Subduction Zones) funded by the Millennium Scientific Initiative (ICM) of the Chilean Government grant NC160025. F.O. acknowledges financial software support from the ESA NoR project ID: 65514, M.M. acknowledges financial support from the FONDECYT Project ANID 1181479.

Institutional Review Board Statement: Not applicable.

Informed Consent Statement: Not applicable.

Data Availability Statement: The geological maps are available on the public portal SERNAGEOMIN, Chilean National Geological and Mining Service. https://www.sernageomin.cl/. GNSS data is available on the platform of Nevada Geodetic Laboratory, of the University of Nevada, NV, USA. http://geodesy.unr.edu/index.php. The catalog of seismic faults is available in the Data Base Chilean active faults, of Millennium Nucleus CYCLO. https://fallasactivas.cl/.

Acknowledgments: F.O. acknowledges academic and technical support of PhD thesis advisor professor Maria Marsella and co-advisor professor Paola Di Mascio. F.O. also acknowledges the financial support from La Sapienza University of Rome (DICEA), Millennium Nucleus CYCLO, and the Department of Civil Engineering of University of Concepcion for doctoral stay. M.M. and J.H. acknowledge support from PRECURSOR ANILLO Project PIA ACT-192169 and FONDECYT Project ANID 1181479.

Conflicts of Interest: The authors declare no conflict of interest.

References

1. Scholz, C.H. *The Mechanics of Earthquakes and Faulting*; Cambridge University Press: Cambridge, UK, 2002; pp. 300–329.
2. DeMets, C.; Gordon, R.G.; Argus, D.F.; Stein, S. Effects of recent revision to the geomagnetic reversal timescale on estimates of current plate motion. *Geophys. Res. Lett.* **1994**, *21*, 2191–2194. [CrossRef]
3. Moreno, M.; Rosenau, M.; Oncken, O. Maule earthquake slip correlates with pre-seismic locking of Andean subduction zone. *Nature* **2010**, *467*, 198–202. [CrossRef] [PubMed]
4. Bedford, J.; Moreno, M.; Baez, J.C.; Lange, D.; Tilmann, F.; Rosenau, M.; Heidbach, O.; Oncken, O.; Bartsch, M.; Rietbrock, A.; et al. A high-resolution, time-variable afterslip model for the 2010 Maule Mw = 8.8, Chile megathrust earthquake. *Earth Planet. Sci. Lett.* **2013**, *383*, 26–36. [CrossRef]
5. Kelson, K.; Witter, R.C.; Tassara, A.; Ryder, I.; Ledezma, C.; Montalva, G.; Frost, D.; Sitar, N.; Moss, R.; Johnson, L. Coseismic Tectonic Surface Deformation during the 2010 Maule, Chile, Mw 8.8 Earthquake. *Earthq. Spectra* **2012**, *28*, 39–54. [CrossRef]
6. Vargas, G.; Farías, M.; Carretier, S.; Tassara, A.; Baize, S.; Melnick, D. Coastal uplift and tsunami effects associated to the 2010 Mw8. 8 Maule earthquake in Central Chile. *Andean Geol.* **2011**, *38*, 219–238.
7. Cecioni, A.; Pineda, V. *Geology and Geomorphology of Natural Hazards and Humand-Induced Disasters in Chile*; Latrubesse, E., Ed.; Elsevier: Amsterdam, The Netherlands, 2009; pp. 379–412.
8. Watts, A.B. Tectonic subsidence, flexure and global changes of sea level. *Nature* **1982**, *297*, 469–474. [CrossRef]
9. Dokka, R.K. Modern-day tectonic subsidence in coastal Louisiana. *Geology* **2006**, *34*, 281–284. [CrossRef]
10. Minderhoud, P.; Middelkoop, H.; Erkens, G.; Stouthamer, E. Groundwater extraction may drown mega-delta: Projections of extraction-induced subsidence and elevation of the Mekong delta for the 21st century. *Environ. Res. Commun.* **2019**, *2*, 011005. [CrossRef]
11. Chen, B.; Gong, H.; Chen, Y.; Li, X.; Zhou, C.; Lei, K.; Zhu, L.; Duan, L.; Zhao, X. Land subsidence and its relation with groundwater aquifers in Beijing Plain of China. *Sci. Total Environ.* **2020**, *735*, 139111. [CrossRef]
12. Guo, L.; Gong, H.; Ke, Y.; Zhu, L.; Li, X.; Lyu, M.; Zhang, K. Mechanism of Land Subsidence Mutation in Beijing Plain under the Background of Urban Expansion. *Remote Sens.* **2021**, *13*, 3086. [CrossRef]
13. Turner, R.E.; Mo, Y. Salt Marsh Elevation limit determined after subsidence from hydrologic change and hydro-carbon extraction. *Remote Sens.* **2021**, *13*, 49. [CrossRef]
14. Singh, A.; Rao, G.S. Crustal structure and subsidence history of the Mannar basin through potential field modelling and backstripping analysis: Implications on basin evolution and hydrocarbon exploration. *J. Pet. Sci. Eng.* **2021**, *206*, 109000. [CrossRef]
15. Gahramanov, G.; Babayev, M.; Shpyrko, S.; Mukhtarova, K. Subsidence history and hydrocarbon migration modeling in south caspian basin. *Visnyk Taras Shevchenko Natl. Univ. Kyiv. Geol.* **2020**, *1*, 82–91. [CrossRef]

16. Stramondo, S.; Bozzano, F.; Marra, F.; Wegmuller, U.; Cinti, F.; Moro, M.; Saroli, M. Subsidence induced by urbanisation in the city of Rome detected by advanced InSAR technique and geotechnical investigations. *Remote Sens. Environ.* **2008**, *112*, 3160–3172. [CrossRef]
17. Manunta, M.; Marsella, M.; Zeni, G.; Sciotti, M.; Atzori, S.; Lanari, R. Two-scale surface deformation analysis using the SBAS-DInSAR technique: A case study of the city of Rome, Italy. *Int. J. Remote Sens.* **2008**, *29*, 1665–1684. [CrossRef]
18. Abidin, H.Z.; Andreas, H.; Djaja, R.; Darmawan, D.; Gamal, M. Land subsidence characteristics of Jakarta between 1997 and 2005, as estimated using GPS surveys. *GPS Solut.* **2008**, *12*, 23–32. [CrossRef]
19. Orellana, F.; Blasco, J.D.; Foumelis, M.; D'Aranno, P.; Marsella, M.; Di Mascio, P. DInSAR for Road Infrastructure Monitoring: Case Study Highway Network of Rome Metropolitan (Italy). *Remote Sens.* **2020**, *12*, 3697. [CrossRef]
20. Chang, L.; Dollevoet, R.P.B.J.; Hanssen, R.F. Monitoring Line-Infrastructure with Multisensor SAR Interferometry: Products and Performance Assessment Metrics. *IEEE J. Sel. Top. Appl. Earth Obs. Remote Sens.* **2018**, *11*, 1593–1605. [CrossRef]
21. Ferretti, A.; Fumagalli, A.; Novali, F.; Prati, C.; Rocca, F.; Rucci, A. A New Algorithm for Processing Interferometric Data-Stacks: SqueeSAR. *IEEE Trans. Geosci. Remote Sens.* **2011**, *49*, 3460–3470. [CrossRef]
22. Ferretti, A.; Prati, C.; Rocca, F. Nonlinear subsidence rate estimation using permanent scatterers in differential SAR interferometry. *IEEE Trans. Geosci. Remote Sens.* **2000**, *38*, 2202–2212. [CrossRef]
23. Lanari, R.; Mora, O.; Manunta, M.; Mallorqui, J.J.; Berardino, P.; Sansosti, E. A small-baseline approach for investigating deformations on full-resolution differential SAR interferograms. *IEEE Trans. Geosci. Remote Sens.* **2004**, *42*, 1377–1386. [CrossRef]
24. Werner, C.; Wegmuller, U.; Strozzi, T.; Wiesmann, A. Interferometric point target analysis for deformation mapping. In Proceedings of the International Geoscience and Remote Sensing symposium (IGARSS), Toulouse, France, 21–25 July 2003; Volume 7, pp. 4362–4364.
25. Bonano, M.; Manunta, M.; Pepe, A.; Paglia, L.; Lanari, R. From Previous C-Band to New X-Band SAR Systems: Assessment of the DInSAR Mapping Improvement for Deformation Time-Series Retrieval in Urban Areas. *IEEE Trans. Geosci. Remote Sens.* **2013**, *51*, 1973–1984. [CrossRef]
26. Casu, F.; Manzo, M.; Lanari, R. A quantitative assessment of the SBAS algorithm performance for surface deformation retrieval from DInSAR data. *Remote Sens. Environ.* **2006**, *102*, 195–210. [CrossRef]
27. Crosetto, M.; Monserrat, O.; Cuevas, M.; Crippa, B. Spaceborne Differential SAR Interferometry: Data Analysis Tools for Deformation Measurement. *Remote Sens.* **2011**, *3*, 305–318. [CrossRef]
28. Bovenga, F.; Nitti, D.O.; Fornaro, G.; Radicioni, F.; Stoppini, A.; Brigante, R. Using C/X-band SAR interferometry and GNSS measurements for the Assisi landslide analysis. *Int. J. Remote Sens.* **2013**, *34*, 4083–4104. [CrossRef]
29. Hilley, G.E.; Bürgmann, R.; Ferretti, A.; Novali, F.; Rocca, F. Dynamics of Slow-Moving Landslides from Permanent Scatterer Analysis. *Science* **2004**, *304*, 1952–1955. [CrossRef]
30. Sansosti, E.; Casu, F.; Manzo, M.; Lanari, R. Space-borne radar interferometry techniques for the generation of deformation time series: An advanced tool for Earth's surface displacement analysis. *Geophys. Res. Lett.* **2010**, *37*, L20305. [CrossRef]
31. Tizzani, P.; Battaglia, M.; Zeni, G.; Atzori, S.; Berardino, P.; Lanari, R. Uplift and magma intrusion at Long Valley caldera from InSAR and gravity measurements. *Geology* **2009**, *37*, 63–66. [CrossRef]
32. Trasatti, E.; Casu, F.; Sansosti, E.; Tizzani, P.; Zeni, G.; Lanari, R.; Giunchi, C.; Pepe, S.; Solaro, G.; Tagliaventi, S.; et al. The 2004–2006 uplift episode at Campi Flegrei caldera (Italy): Constraints from SBAS-DInSAR ENVISAT data and Bayesian source inference. *Geophys. Res. Lett.* **2008**, *35*, L07308. [CrossRef]
33. Goorabi, A.; Karimi, M.; Yamani, M.; Perissin, D. Land subsidence in Isfahan metropolitan and its relationship with geological and geomorphological settings revealed by Sentinel-1A InSAR observations. *J. Arid. Environ.* **2020**, *181*, 104238. [CrossRef]
34. Hernandez, J.A.C.; Lazecký, M.; Šebesta, J.; Bakoň, M. Relation between surface dynamics and remote sensor InSAR results over the Metropolitan Area of San Salvador. *Nat. Hazards* **2020**, *103*, 3661–3682. [CrossRef]
35. Cigna, F.; Tapete, D. Present-day land subsidence rates, surface faulting hazard and risk in Mexico City with 2014–2020 Sentinel-1 IW InSAR. *Remote Sens. Environ.* **2021**, *253*, 112161. [CrossRef]
36. Xu, B.; Feng, G.; Li, Z.; Wang, Q.; Wang, C.; Xie, R. Coastal subsidence monitoring associated with land reclamation using the point target based SBAS-InSAR method: A case study of Shenzhen, China. *Remote Sens.* **2016**, *8*, 652. [CrossRef]
37. Di Paola, G.; Alberico, I.; Aucelli, P.; Matano, F.; Rizzo, A.; Vilardo, G. Coastal subsidence detected by Synthetic Aperture Radar interferometry and its effects coupled with future sea-level rise: The case of the Sele Plain (Southern Italy). *J. Flood Risk Manag.* **2018**, *11*, 191–206. [CrossRef]
38. Hao, Q.N.; Takewaka, S. Detection of Land Subsidence in Nam Dinh Coast by Dinsar Analyses. In Proceedings of the International Conference on Asian and Pacific Coasts, Hanoi, Vietnam, 25–28 September 2019; Springer: Singapore, 2019; pp. 1287–1294.
39. Anzidei, M.; Scicchitano, G.; Scardino, G.; Bignami, C.; Tolomei, C.; Vecchio, A.; Serpelloni, E.; de Santis, V.; Monaco, C.; Milella, M.; et al. Relative Sea-Level Rise Scenario for 2100 along the Coast of South Eastern Sicily (Italy) by InSAR Data, Satellite Images and High-Resolution Topography. *Remote Sens.* **2021**, *13*, 1108. [CrossRef]
40. Wang, H.; Wright, T.; Yu, Y.; Lin, H.; Jiang, L.; Li, C.; Qiu, G. InSAR reveals coastal subsidence in the Pearl River Delta, China. *Geophys. J. Int.* **2012**, *191*, 1119–1128. [CrossRef]
41. Du, Y.; Feng, G.; Peng, X.; Li, Z.-W. Subsidence Evolution of the Leizhou Peninsula, China, Based on InSAR Observation from 1992 to 2010. *Appl. Sci.* **2017**, *7*, 466. [CrossRef]

42. Hu, B.; Chen, J.; Zhang, X. Monitoring the Land Subsidence Area in a Coastal Urban Area with InSAR and GNSS. *Sensors* **2019**, *19*, 3181. [CrossRef]
43. Zinno, I.; Elefante, S.; Mossucca, L.; de Luca, C.; Manunta, M.; Terzo, O.; Lanari, R.; Casu, F. A First Assessment of the P-SBAS DInSAR Algorithm Performances Within a Cloud Computing Environment. *IEEE J. Sel. Top. Appl. Earth Obs. Remote Sens.* **2015**, *8*, 4675–4686. [CrossRef]
44. Zinno, I.; Casu, F.; de Luca, C.; Elefante, S.; Lanari, R.; Manunta, M. A Cloud Computing Solution for the Efficient Implementation of the P-SBAS DInSAR Approach. *IEEE J. Sel. Top. Appl. Earth Obs. Remote Sens.* **2017**, *10*, 802–817. [CrossRef]
45. Manunta, M.; de Luca, C.; Zinno, I.; Casu, F.; Manzo, M.; Bonano, M.; Lanari, R. The parallel SBAS approach for Sentinel-1 interferometric wide swath deformation time-series generation: Algorithm description and products quality assessment. *IEEE Trans. Geosci. Remote Sens.* **2019**, *57*, 6259–6281. [CrossRef]
46. Lanari, R.; Bonano, M.; Casu, F.; de Luca, C.; Manunta, M.; Manzo, M.; Onorato, G.; Zinno, I. Automatic Generation of Sentinel-1 Continental Scale DInSAR Deformation Time Series through an Extended P-SBAS Processing Pipeline in a Cloud Computing Environment. *Remote Sens.* **2020**, *12*, 2961. [CrossRef]
47. Berardino, P.; Fornaro, G.; Lanari, R.; Sansosti, E. A new algorithm for surface deformation monitoring based on small baseline differential SAR interferograms. *IEEE Trans. Geosci. Remote Sens.* **2002**, *40*, 2375–2383. [CrossRef]
48. Manunta, M.; Casu, F.; Zinno, I.; de Luca, C.; Pacini, F.; Brito, F.; Blanco, P.; Iglesias, R.; Lopez, A.; Briole, P.; et al. The Geohazards Exploitation Platform: An advanced cloud-based environment for the Earth Science community. In Proceedings of the19th EGU General Assembly, EGU2017, Vienna, Austria, 23–28 April 2017; p. 14911.
49. Foumelis, M.; Papadopoulou, T.; Bally, P.; Pacini, F.; Provost, F.; Patruno, J. Monitoring Geohazards Using On-Demand and Systematic Services on Esa's Geohazards Exploitation Platform. In Proceedings of the IGARSS 2019, IEEE International Geoscience and Remote Sensing Symposium, Yokohama, Japan, 28 July–2 August 2019; IEEE: Piscataway, NJ, USA, 2019; pp. 5457–5460.
50. Galve, J.P.; Pérez-Peña, J.V.; Azañón, J.M.; Closson, D.; Calò, F.; Reyes-Carmona, C.; Jabaloy, A.; Ruano, P.; Mateos, R.M.; Notti, D.; et al. Evaluation of the SBAS InSAR Service of the European Space Agency's Geohazard Exploitation Platform (GEP). *Remote Sens.* **2017**, *9*, 1291. [CrossRef]
51. Reyes-Carmona, C.; Galve, J.P.; Barra, A.; Monserrat, O.; María Mateos, R.; Azañón, J.M.; Perez-Pena, J.V.; Ruano, P. The Sentinel-1 CNR-IREA SBAS service of the European Space Agency's Geohazard Exploitation Platform (GEP) as a powerful tool for landslide activity detection and monitoring. In Proceedings of the EGU General Assembly, Vienna, Austria, 3–8 May 2020; p. 19410.
52. Sippl, C.; Moreno, M.; Benavente, R. Microseismicity Appears to Outline Highly Coupled Regions on the Central Chile Megathrust. *J. Geophys. Res. Solid Earth* **2021**, *126*, 022252. [CrossRef]
53. Maldonado, V.; Contreras, M.; Melnick, D. A comprehensive database of active and potentially-active continental faults in Chile at 1:25,000 scale. *Sci. Data* **2021**, *8*, 20. [CrossRef]
54. Farías, M.; Comte, D.; Roecker, S.W.; Carrizo, D.; Pardo, M. Crustal extensional faulting triggered by the 2010 Chilean earthquake: The Pichilemu Seismic Sequence. *Tectonics* **2011**, *30*, TC6010. [CrossRef]
55. Gana, P.; Wall, R.; Gutiérrez, A. Mapa Geológico del Área de Valparaíso- Curacaví. Regiones de Valparaíso y Metropolitana. In *Mapa Geológico*; Servicio Nacional de Geología y Minería: Santiago, Chile, 1996; pp. 1–19.
56. SERNAGEOMN—National Geology and Mining Service, Source Open Geological Map of Chile. Available online: https://www.sernageomin.cl/geologia/ (accessed on 13 October 2021).
57. Wall, R.M.; Lara, L.E.; Pérez de Arce, C. *Upper Pliocene-Lower Pleistocene 40 Ar/39 Ar Ages of Pudahuel Ignimbrite (Diamante-Maipo volcanic complex), Central Chile (33.5 0 S)*; International Atomic Energy Agency (IAEA): Vienna, Austria, 2001.
58. Piracés, R. Estratigrafía de la Cordillera de la Costa entre la cuesta El Melón y Limache, Provincia de Valparaíso, Chile. In Proceedings of the Congreso Geológico Chileno, Santiago, Chile, 2–7 August 1976.
59. Vergara, M.; Nystrom, J.O. Geochemical features of Lower Cretaceous back-arc lavas in the Andean Cordillera, Central Chile (31–34°S). *Rev. Geológica Chile* **1996**, *23*, 97–106.
60. Thomas, H. Geología de la Cordillera de la Costa entre el valle de la Ligua y la cuesta Barriga. In *Santiago*; Instituto de Investigaciones Geológicas: Santiago, Chile, 1958; p. 86.
61. Levi, B.; Aguirre, L.; Nyström, J.O.; Padilla, H.; Vergara, M. Low-grade regional metamorphism in the Mesozoic-Cenozoic volcanic sequences of the Central Andes. *J. Metamorph. Geol.* **1989**, *7*, 487–495. [CrossRef]
62. ESA Sentinel—Topsar Processing. Available online: https://sentinel.esa.int/web/sentinel/technical-guides/sentinel-1-sar/products-algorithms/level-1-algorithms/topsar-processing (accessed on 25 July 2021).
63. Blewitt, G.; Hammond, W.C.; Kreemer, C. Harnessing the GPS Data Explosion for Interdisciplinary Science. *Eos* **2018**, *99*, 485. [CrossRef]
64. Rebischung, P.; Griffiths, J.; Ray, J.; Schmid, R.; Collilieux, X.; Garayt, B. IGS08: The IGS realization of ITRF2008. *GPS Solut.* **2011**, *16*, 483–494. [CrossRef]
65. Bevis, M.; Brown, A.G.P. Trajectory models and reference frames for crustal motion geodesy. *J. Geod.* **2014**, *88*, 283–311. [CrossRef]
66. Casu, F.; Elefante, S.; Imperatore, P.; Zinno, I.; Manunta, M.; de Luca, C.; Lanari, R. SBAS-DInSAR parallel processing for deformation time-series computation. *IEEE J. Sel. Top. Appl. Earth Obs. Remote Sens.* **2014**, *7*, 3285–3296. [CrossRef]
67. Farr, T.G.; Rosen, P.A.; Caro, E.; Crippen, R.; Duren, R.; Hensley, S.; Kobrick, M.; Paller, M.; Rodriguez, E.; Roth, L.; et al. The Shuttle Radar Topography Mission. *Rev. Geophys.* **2007**, *45*, RG2004. [CrossRef]

68. Yague-Martinez, N.; de Zan, F.; Prats-Iraola, P. Coregistration of Interferometric Stacks of Sentinel-1 TOPS Data. *IEEE Geosci. Remote Sens. Lett.* **2017**, *14*, 1002–1006. [CrossRef]
69. Cigna, F.; Tapete, D. Sentinel-1 Big Data Processing with P-SBAS InSAR in the Geohazards Exploitation Platform: An Experiment on Coastal Land Subsidence and Landslides in Italy. *Remote Sens.* **2021**, *13*, 885. [CrossRef]
70. Crosetto, M.; Monserrat, O.; Cuevas-González, M.; Devanthéry, N.; Crippa, B. Persistent scatterer interferometry: A review. *ISPRS J. Photogramm. Remote Sens.* **2016**, *115*, 78–89. [CrossRef]
71. Aron, F.; Allmendinger, R.W.; Cembrano, J.; González, G.; Yáñez, G. Permanent fore-arc extension and seismic segmentation: Insights from the 2010 Maule earthquake, Chile. *J. Geophys. Res. Solid Earth* **2013**, *118*, 724–739. [CrossRef]
72. Aron, F.; Cembrano, J.; Astudillo, F.; Allmendinger, R.W.; Arancibia, G. Constructing forearc architecture over megathrust seismic cycles: Geological snapshots from the Maule earthquake region, Chile. *GSA Bull.* **2014**, *127*, 464–479. [CrossRef]
73. Ruiz, S.; Metois, M.; Fuenzalida, A.; Ruiz, J.; Leyton, F.; Grandin, R.; Vigny, C.; Madariaga, R.; Campos, J. Intense foreshocks and a slow slip event preceded the 2014 Iquique Mw8.1 earthquake. *Science* **2014**, *345*, 1165–1169. [CrossRef]
74. Ryder, I.; Rietbrock, A.; Kelson, K.; Bürgmann, R.; Floyd, M.; Socquet, A.; Vigny, C.; Carrizo, D. Large extensional aftershocks in the continental forearc triggered by the 2010 Maule earthquake, Chile. *Geophys. J. Int.* **2012**, *188*, 879–890. [CrossRef]
75. Martínez, C.; Grez, P.W.; Martín, R.A.; Acuña, C.E.; Torres, I.; Contreras-López, M. Coastal erosion in sandy beaches along a tectonically active coast: The Chile study case. *Prog. Phys. Geogr. Earth Environ.* **2021**. [CrossRef]
76. Muñoz, J.J.; Melnick, D.; Brill, D.; Strecker, M.R. Segmentation of the 2010 Maule Chile earthquake rupture from a joint analysis of uplifted marine terraces and seismic-cycle deformation patterns. *Quat. Sci. Rev.* **2015**, *113*, 171–192. [CrossRef]
77. Calle-Gardella, D.; Comte, D.; Farías, M.; Roecker, S.; Rietbrock, A. Three-dimensional local earthquake tomography of pre-Cenozoic structures in the coastal margin of central Chile: Pichilemu fault system. *J. Seism.* **2021**, *25*, 521–533. [CrossRef]
78. Santibáñez, I.; Cembrano, J.; García-Pérez, T.; Costa, C.; Yáñez, G.; Marquardt, C.; Arancibia, G.; González, G. Crustal faults in the Chilean Andes: Geological constraints and seismic potential. *Andean Geol.* **2018**, *46*, 32–65. [CrossRef]